



Acid and redox activity of template-free Al-rich H-BEA⁺ and Fe-BEA⁺ zeolites



Petr Sazama^{a,*}, Blanka Wichterlová^a, Štěpán Sklenák^a, Vasile I. Parvulescu^b, Natalia Candu^b, Galina Sádovská^a, Jiří Dědeček^a, Petr Klein^a, Veronika Pashkova^a, Petr Šťastný^a

^aJ. Heyrovský Institute of Physical Chemistry, Academy of Sciences of the Czech Republic, CZ-182 23 Prague 8, Czech Republic

^bUniversity of Bucharest, Department of Organic Chemistry and Catalysis, B-dul Regina Elisabeta 4-12, 030016 Bucharest, Romania

ARTICLE INFO

Article history:

Received 5 May 2014

Revised 18 June 2014

Accepted 21 June 2014

Available online 13 August 2014

Keywords:

Beta (BEA⁺) zeolite

Acid strength

Cracking of decane

Alkylation of aromatics

Hydroamination of styrene with aniline

Iron zeolites

Fe-beta

NH₃-SCR-NO_x

Decomposition of N₂O

ABSTRACT

Al-rich template-free BEA⁺ zeolite (Si/Al 4.6) was synthesized and its structure was analyzed in comparison with the conventional H-BEA⁺ zeolite of Si/Al 11.3 using XRD, N₂ sorption, SEM, FTIR, ²⁷Al 3Q and ²⁹Si MAS NMR spectroscopy, and DFT calculation of the deprotonation energies. The Al-rich H-BEA⁺ exhibited a high concentration of Brønsted and Lewis sites, both of high acid strength, although AlSiAl sequences were present in the framework. In Al-rich Fe-BEA⁺ the exchanged Fe ions, Fe-oxo species, and Fe-oxo oligomers were identified by UV-vis spectroscopy. Cracking of *n*-decane, alkylation of benzene with benzyl alcohol and hydroamination of styrene with aniline to (*anti*)Markovnikov phenyl-[2-phenylethyl]amine over H-BEA⁺, and decomposition of N₂O and NH₃-SCR-NO_x over Fe-BEA⁺ were investigated in relation to the concentration and nature of acid and Fe-redox sites. The high concentration of Al-related active sites and the highly regular structure of Al-rich beta zeolite are directly manifested in enhanced activity compared with conventional Si-rich beta zeolite.

© 2014 Elsevier Inc. All rights reserved.

1. Introduction

High-silica zeolites possessing strongly acidic protons, such as dealuminated faujasites, mordenites, MFI, and beta (BEA⁺) zeolites, represent important zeolite structures employed as catalysts in fluid catalytic cracking and hydrocracking units converting oil fractions to valuable gasoline and diesel fuels, as well as in production of petrochemicals [1]. In addition, cationic species in zeolites with low Al concentrations with MFI, BEA⁺, or FER topologies exhibit extraordinary redox behavior employed in selective oxidation of hydrocarbons [2], selective conversion of N₂O/NO/NO₂ to molecular nitrogen by N₂O decomposition [3], and SCR of NO/NO₂ using NH₃ [4] or hydrocarbons [5], employed in the end-pipe gases of chemical plants, electric power stations, and exhaust gases of diesel engines.

Zeolite beta (BEA⁺, consisting of three A, B, and C polymorphs) [6] is assembled from 4-, 5-, and 6-membered rings forming an intersecting three-dimensional (3D) channel structure with 12-membered ring openings of 6.6 × 6.7 Å (Fig. 1). Its larger 3D 12-ring inner pores compared to 10-ring pores in MFI, only

monodimensional 12-ring pores of MOR, and absence of cavities existing in Y zeolites represent a great advantage for fast diffusion of bulkier molecules participating in oil processing, dewaxing and isomerization of paraffins, and benzene alkylation with low olefins, as well as organic specialty manufacturing. However, a substantial shortcoming for wider industrial application of the beta zeolite is the need to use expensive tetraethylammonium hydroxide (TEAOH) as a template for its hydrothermal synthesis, providing the beta framework for Si/Al > 11.

Since 2008, the successful synthesis of the template-free and Al-rich beta zeolite with Si/Al ~ 4.5 was reported by Xie et al. [7], Majano et al. [8], Kamimura et al. [9], and Kubota et al. [10] using calcined beta seeds added to the aluminosilicate gel. These procedures yielded a beta zeolite of high crystallinity and well-developed crystallites with dimensions about 0.3–0.5 μm. As could be expected, the increased concentration of Al in the beta zeolite with Si/Al ~ 4.5 obtained by the template-free route is accompanied by an increased ion-exchange capacity for protons, metal cations, and metal-oxo complexes.

Very recently, a collaborative effort among several laboratories [11,12] yielded a comparison of the structure, framework Al, and crystal size of the Al-rich beta zeolite (Si/Al 4.6) obtained by template-free synthesis with those of the standard BEA⁺ (Si/Al

* Corresponding author.

E-mail address: petr.sazama@jh-inst.cas.cz (P. Sazama).

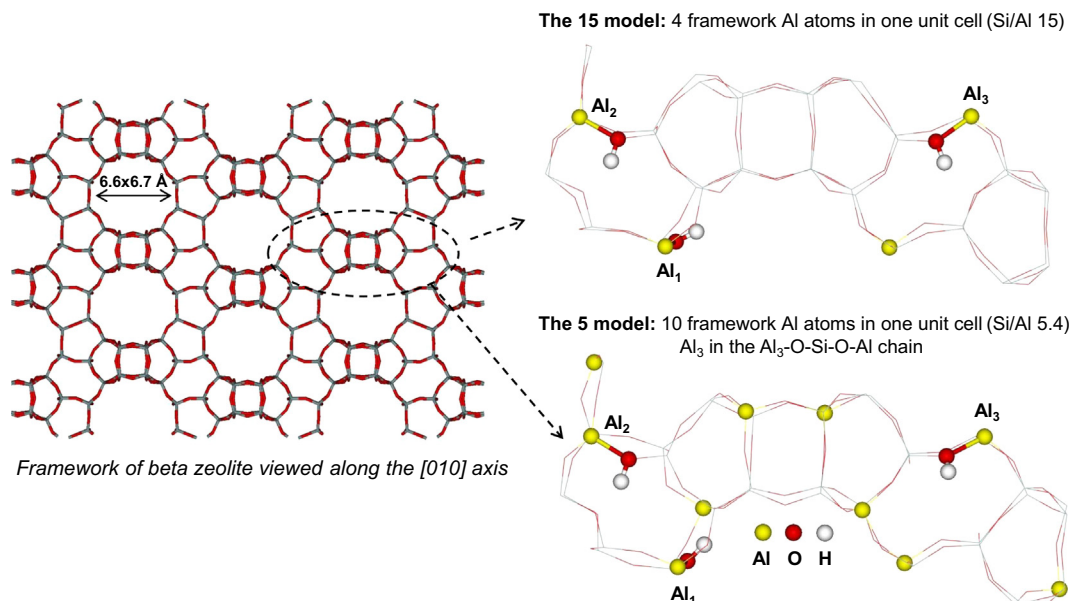


Fig. 1. Illustration of the structure of the beta zeolite and structural models of the zeolite with 4 and 10 Al atoms in one unit cell (molar Si/Al ratio of 15 and 5.4, respectively) used for the calculation of deprotonation energies of the corresponding Brønsted acid sites.

12) synthesized using TMAOH and of their activities in several acid-catalyzed reactions (hydrocarbon alkylation, hydroisomerization, and acylation). The authors showed that, in addition to the higher concentration of Al in the framework, the template-free beta zeolite exhibited more regular crystalline structure and slightly larger crystals (0.3–0.5 μm). While the larger crystals were connected with faster zeolite deactivation in benzene alkylation with ethylene, the higher concentration of strong acid sites greatly increased yields of cracked products in *n*-decane hydrocracking at low temperatures. Low activity in the acylation of anisole with acetic anhydride was observed over the Al-rich BEA⁺ and its dealumination to Si/Al 9 was necessary for a high 54% yield of *p*-methoxyacetophenone at 99% selectivity due to transport limitations [13]. Kubota et al. [10] showed that steaming of Al-rich BEA followed by partial dealumination using nitric acid provides a selective catalyst for high-temperature cracking of hexane to propene.

The results obtained to date on the activity of template-free BEA⁺ in acid-catalyzed reactions raised new questions on (i) the strength of bridging OH groups in Al-rich BEA⁺, (ii) the structure and concentration of the metal counter-ions and metal-oxo species, and (iii) the related activity of H- and metal-Al-rich BEA⁺ zeolite in acid- and redox-catalyzed reactions.

In the present study, we compare the synthesized template-free BEA⁺ (Si/Al 4.6) and commercial beta zeolite (Si/Al 11.3, synthesized using TMAOH) with respect to (i) the concentration and strength of the protonic Brønsted sites and the occurrence of Lewis sites, (ii) the ion-exchange capacity for Fe ions and Fe-oxo complexes, and (iii) the crystal size and texture. These parameters are related to the activity and selectivity of BEA⁺ zeolites with quite different Al content in their H-form for acid-catalyzed and Fe-BEA⁺ in redox-catalyzed reactions. In this respect, it is demonstrated that enhancement is attained in cracking of *n*-decane to olefins and paraffins as well as transformation of bulkier molecules, the precursors for synthesis of natural products, pharmaceuticals, cosmetics, etc. In the alkylation of benzene by benzyl alcohol to diphenylmethane and hydroamination of styrene with aniline, the shape-selective effects, crystal size, and diffusion constraints are considered in addition to the increased concentrations of active acid sites. For redox-catalyzed reactions, we demonstrate a marked increase in the concentration of Fe ions and Fe-oxo species and an

enhancement of the activity of Al-rich Fe-BEA⁺ compared to conventional Si-rich Fe-BEA⁺ in N₂O decomposition and NH₃-SCR-NO_x to molecular nitrogen.

2. Experimental

2.1. Preparation of H-BEA⁺ and FeH-BEA⁺

Al-rich beta zeolite was hydrothermally synthesized by a procedure based on the reports in Refs. [7–9,14] using seeding of calcined beta crystals of Si/Al 11.5 (TZB-212, Tricat) in an amount of 0.052 g per 1 g SiO₂. A starting aluminosilicate mixture with a molar ratio of Al₂O₃/SiO₂/NaOH/H₂O 1:26.2:17.2:911 was prepared from NaAlO₂ and fumed silica (Cabosil). An amount of 10 g NaAlO₂ was dissolved in 1000 ml deionized water followed by addition of 42 g NaOH, stirring for 40 min, addition of 96 g silica, stirring for 10 min, and addition of 5 g of beta zeolite seeds, after which mixture homogenization took place for 5 min at room temperature. The mixture was treated hydrothermally at 120 °C for 125 h in a 2500-ml autoclave with very slow stirring under autogenic pressure. The obtained solid product was separated by filtration, washed with deionized water, and dried at 80 °C for 6 h. The zeolite product has a molar Si/Al ratio of 4.6 and was denoted as BEA-5. The BEA-5 sample was ion-exchanged three times with 1.0 M NH₄NO₃, yielding NH₄-BEA-5 and, after deammonization at 500 °C, obtaining H-BEA-5. The beta zeolite (containing template) with Si/Al 11.3 was kindly supplied by Zeolyst International (CP 814B -25, Lot. No. 814B-25-1597-77). This type of beta sample is widely used for preparation of zeolite catalysts and as a standard for comparing the activities of various zeolites. The sample denoted as BEA-11 was prepared from this zeolite by calcination in an ammonia stream at 420 °C for 8 h to remove the template, according to the procedure first described by Creighton et al. [15]. This procedure yields a charge balance of the framework AlO₄⁻ by NH₄⁺ ions and thus preserves Al in the framework sites [16]. The NH₄-BEA-11 was deammoniated by calcination in a stream of O₂ at 520 °C for 2 h to H-BEA-11. The chemical compositions of both H-BEA⁺ samples are given in Table 1. Na-forms of beta zeolites for NMR measurements were obtained by Na⁺ ion exchange with NaNO₃ of part of the NH₄-BEA-5 and H-BEA-11.

Table 1
Characteristics of beta zeolites.

Sample	Si/Al ^a	c_{Al}^a			S	V_{mi}^d	S_{mi}^e	S_{EXT}
		(mmol g ⁻¹)						
H-BEA-11	11.3	1.35	0.78	0.25	617	0.169	333	284
H-BEA-5	4.6	2.97	1.43	0.73	482	0.243	470	12

^a From chemical analysis.

^{b,c} Concentrations of acid Brønsted and Lewis sites, respectively, from FTIR spectra of adsorbed *d*₃-acetonitrile.

^d Microporous volume.

^e Hypothetical surface area in micropores.

Fe-BEA-5 (11.7 wt.% Fe, Fe/Al 0.73) and Fe-BEA-11 (5.3 wt.% Fe/Al 0.77) were prepared by ion exchange of the respective BEA⁺ zeolites with aqueous Fe(II)SO₄ solution under nitrogen. Two grams of the beta zeolite was slurried in 50 ml of deoxygenated distilled water. Then 7 g of Fe(II)SO₄ · 7H₂O was added in the form of a pressed pellet. The exchange proceeded for 14 h at 95 °C under nitrogen. The slurry was then filtered and the Fe-zeolite was washed with deoxygenated distilled water and dried under nitrogen followed by heating (2 °C/min) in a stream of nitrogen at up to 500 °C maintained for 3 h.

2.2. Structural analysis

Zeolites were characterized by XRD recorded by a Bruker D8 instrument, Bruker AXS, U.S.A., N₂ sorption at 77 K obtained on an ASAP2020 Micromeritics apparatus, and scanning electron microscopy (SEM) using a Jeol JSM-03 instrument. The ²⁷Al MAS and ²⁷Al 3Q MAS NMR spectra were measured on a Bruker Avance 500 MHz (11.7 T) Wide Bore spectrometer using ZrO₂ rotors with a rotation speed of 12 kHz. Chemical shifts were referenced to the aqueous solution of Al(NO₃)₃. For the ²⁷Al MAS NMR experiment, high-power decoupling pulse sequences with a $\pi/12\pi$ (0.7 μ s) excitation pulse and 1 s relaxation delay were applied to fully hydrated samples. ²⁷Al 3Q experiments were performed using the two-pulse z-filtered procedure. A π pulse was used for excitation and a $\pi/3$ pulse for conversion. Pulses were individually optimized for each sample. The relaxation delay was 0.5 s. The presented 2D contour plots are the result of a 2D Fourier transformation followed by a shearing transformation. Thus, the F1 axis is the isotropic dimension and F2 gives the MAS spectrum containing the second-order quadrupolar line shape. Isotropic chemical shifts were obtained from the first moment analysis of the 2D plot using the following relationship:

$$\delta_{\text{iso}} = (17\delta_{\text{F1}} + 10\delta_{\text{F2}})/27.$$

²⁹Si MAS NMR single pulse and cross-polarization spectra were measured at a rotation speed of 5 kHz, with a $\pi/6$ (1.7 μ s) excitation pulse and a relaxation delay of 30 s for single pulse spectra. For the cross-polarization spectra, pulse sequences with 50% ramp CP pulse, 2000 μ s contact time, high-power decoupling, and 5 s relaxation delay were employed. ²⁹Si high-power decoupling spectra were decomposed to the Gaussian bands using Microcall Origin 4.1 software (Microcall Software Inc., USA). The framework aluminum content (Si/Al_{FR}) was estimated according to the formula

$$\text{Si/Al}_{\text{FR}} = I/(0.25I_1 + 0.5I_2),$$

where *I*₁ denotes the intensity of the NMR lines corresponding to the Si(3Si,1Al), *I*₂ that of those corresponding to the Si(2Si,2Al) building unit, and *I* the total ²⁹Si intensity; for details see Ref. [17].

The concentrations of acidic Brønsted and Al-Lewis sites in H-BEA zeolites were determined by adsorption of *d*₃-acetonitrile (13 mbar) on zeolite samples evacuated at 500 °C, carried out at 298 K with subsequent evacuation for 15 min at RT. The IR spectra were recorded on a Nicolet 6700 FTIR spectrometer operating at a

resolution of 1 cm⁻¹ by collecting 256 scans for a single spectrum. The extinction coefficients for C≡N vibrations associated with Brønsted (2298 cm⁻¹, $\epsilon = 2.05 \text{ cm} \mu\text{mol}^{-1}$) and Al-Lewis sites (2325 cm⁻¹, $\epsilon = 3.6 \text{ cm} \mu\text{mol}^{-1}$) were taken from Ref. [18].

The UV–vis–NIR reflectance spectra of hydrated Fe-BEA-5 and -11 were recorded on a Perkin–Elmer Lambda 950 UV–vis–NIR spectrometer equipped with an integrating sphere for diffuse-reflectance measurements covered with Spectralon. Spectralon also served as a reference.

The reflectances were recalculated using the Schuster–Kubelka–Munk function $F(R_{\infty}) = (1 - R_{\infty})^2/2R_{\infty}$, where R_{∞} is the diffuse reflectance from a semi-infinite layer. $F(R_{\infty})$ is proportional to the absorption coefficient for $F(R_{\infty}) < 0.5$. As $F(R_{\infty})$ of Fe samples substantially exceed this value in the UV region, $F(R_{\infty})$ were corrected using a correction coefficient χ/η ($\chi/\eta = 1-1.2$ for $F(R_{\infty}) = 0-10$) derived by Klier [19]. The absorption intensities of the samples were expressed as $F(R_{\infty})_{\text{COR}} = F(R_{\infty}) \cdot (3\chi/8\eta)$, where 3/8 is the conversion coefficient between true absorption and true scattering coefficient and $F(R_{\infty})$.

2.3. Computational details

2.3.1. Structural models of the beta zeolite

Two models of the beta zeolite with P1 symmetry were used to investigate the effect of Si/Al on the deprotonation energies. The first model (hereafter the 15 model) features 4 Al atoms in one unit cell (Si/Al 15) and the second model (hereafter the 5 model) contains 10 Al atoms in one unit cell (Si/Al 5.4) (Fig. 1). All the AlO₄⁻ entities are compensated for by protons in the AlOHSi groups. The Al₁, Al₂, and Al₃ atoms are substituted for in both the models in the same framework positions to allow comparison of the deprotonation energies. According to our previous experimental studies on the distribution of Al atoms in beta zeolites with Si/Al > 11 [16], two different distributions of the framework Al atoms in two double 6MR units were chosen in the 15 model. One double 6MR cage features two Al atoms (Al₁ and Al₂) forming an Al₁SiAl₂ sequence in one 6MR (Fig. 2A), while the other double-6MR unit contains two single Al atoms (one of them is Al₃) located in two 6MRs (Fig. 2B). Two variants of the distribution of Al in the 5 model were employed. Both feature the same location of the Al₁SiAl₂ sequence in one 6MR as in the 15 model: however, the Al₁ and Al₂ atoms also form Al₁SiAl and Al₂SiAl sequences in addition to creating Al₁SiAl₂ as in the 15 model (Fig. 2A). The Al₃ atom forms an Al₃SiAl sequence in variant 1 (Fig. 2B), while the Al₃ atom is a single Al atom in variant 2. AlSiAl sequences were employed in the 5 model, since the Si(2Si,2Al) atoms were observed by ²⁹Si MAS NMR in BEA-5 (see Fig. 3). The starting geometry of both the models was generated from the experimental orthorhombic structure of polymorph A of the beta zeolite (see <http://www.iza-structure.org/databases>: space group, P4122; cell parameters, *a* = 12.632, *b* = 12.632, *c* = 26.186 Å). Details of the electronic structure calculations, geometry optimizations, and molecular dynamics are given in Supplement I.

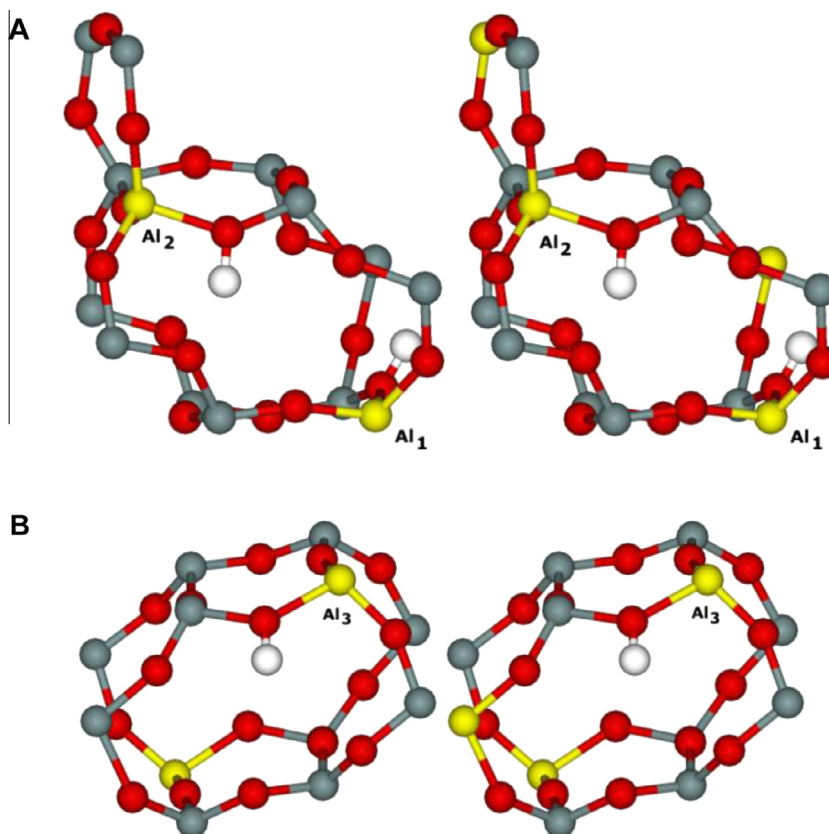


Fig. 2. (A) Positions of the Al₁ and Al₂ atoms forming an Al₁SiAl₂ sequence in a double-6MR: The 15 model (left) and the 5 model (right). In the 5 model, the Al₁ and Al₂ atoms form Al₁SiAl and Al₂SiAl sequences, besides creating Al₁SiSiAl₂. Si atoms are in gray, Al atoms in yellow, O atoms in red, and H atoms in white. (B) Positions of single Al₃ atoms in a double-6MR: The 15 model and the 5 model, variant 2 with a single Al₃ atom (left) and the 5 model, variant 1 with Al₃SiAl (right). (For interpretation of the references to color in this figure legend, the reader is referred to the web version of this article.)

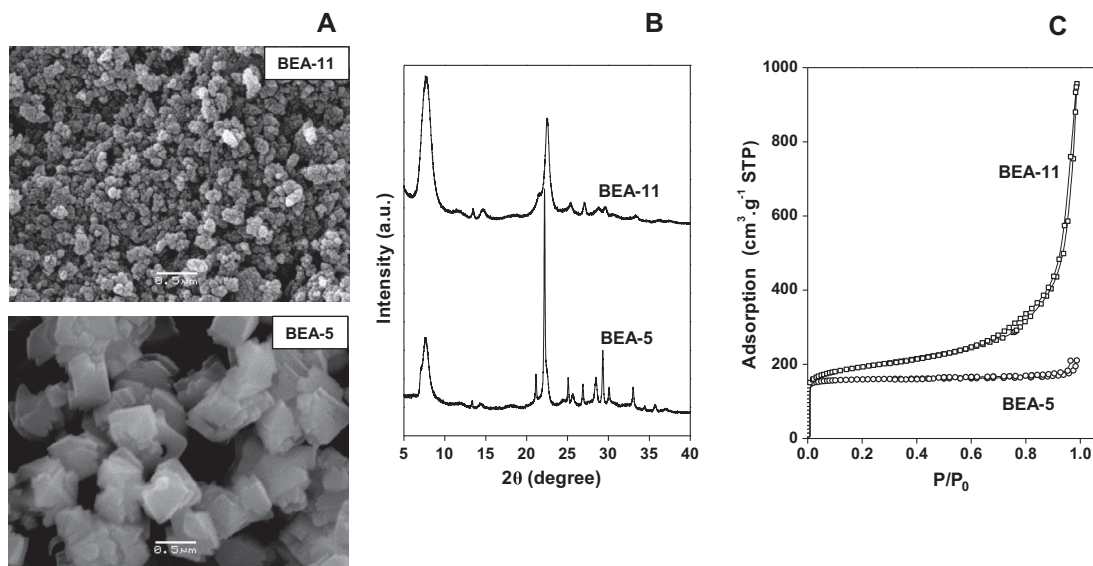


Fig. 3. Characteristics of beta zeolites. (A) SEM micrographs, (B) X-ray diffraction patterns, and (C) N₂-sorption isotherms at 77 K.

2.3.2. Deprotonation energy

The deprotonation energies of the three protons compensating for the three Al atoms that are common to the 15 and 5 models were calculated using the equation $Z - H \rightarrow Z^- + H^+$ [20–22]. The calculated deprotonation energies are a measure of the acidity of

the corresponding Brønsted sites [20–22]. Details regarding calculation of the deprotonation energies employing periodic methods are discussed elsewhere [21]. The differences between two deprotonation energies (i.e., relative deprotonation energies) are used to compare the acidity of the corresponding two Brønsted sites.

2.4. Catalytic reactions

2.4.1. Cracking of *n*-decane

n-Decane cracking was carried out in a fixed-bed flow-through reactor at 480–520 °C and atmospheric pressure. The flow rate of *n*-decane was 1.62×10^{-6} mol s⁻¹ at a He/decane molar ratio of 29 and with typical catalyst weight of 14 mg, corresponding to WHSV 120 h⁻¹. The reaction products were analyzed by an on-line connected Agilent 6890 gas chromatograph equipped with an Al₂O₃/KCl capillary column and a flame ionization detector.

2.4.2. Alkylation of benzene by benzyl alcohol to diphenylmethane

Benylation of benzene to diphenylmethane was performed as follows: Benzene (20 or 50 mmol) was mixed with benzyl alcohol (20 mmol) in a 20 ml glass vial. The dried catalyst (150 mg) was added to this mixture, which was then heated and kept at 80 °C with stirring (1400 rpm) for 2–24 h. After the reaction, the catalyst was filtered out and the reaction mixture was analyzed by FID-GC and MS-GC chromatography (Thermo Electron Corporation Instrument). Both reagents were from Sigma–Aldrich ($\geq 99.0\%$).

2.4.3. Hydroamination of styrene with aniline to phenyl-[2-phenylethyl]amine and phenyl-[1-phenylethyl]amine

Hydroamination of styrene with aniline was performed in a stainless steel autoclave loaded with 50 mg of catalyst, by using 1 mmol aniline and 2 mmols styrene under autogenic pressure at 150 °C. Toluene (4 ml), a non-polar aprotic solvent, was used. The reactants and products were analyzed by GC–MS using a Trace GC 2000 instrument coupled with DSQ MS from Thermo Electron Corporation. The structure of the resulting products was confirmed by ¹H and ¹³C NMR spectroscopy using a Bruker AV 400 spectrometer. Analytical data for the (*anti*)-Markovnikov adduct are given in Supplement II.

2.4.4. Selective catalytic reduction of NO_x by ammonia

Selective catalytic reduction was carried out with catalysts located in a quartz tubular down-flow reactor and using the reactant gases (NO, NH₃, and O₂) and the carrier gas (He). The concentrations of reactants and products were read stepwise at steady state at temperatures from 500 to 200 °C using an UV photometric analyzer (ABB AO2000-Limas11UV) for NO, NO₂, and NH₃ and an infrared absorption photometer (ABB Uras26 EL3020) for N₂O. The experimental conditions for the SCR reaction were as follows: total gas flow rate 350 cm³ min⁻¹ and catalyst weight 20.5 mg corresponding to GHSV 510,000 h⁻¹; NO 500 ppm; NH₃ 520 ppm; O₂ 2%; balance He. NO_x conversion was defined as the reduction of NO and NO₂ to N₂. The concentration of N₂O in the products in all cases was <2 ppm.

2.4.5. Decomposition of N₂O

Decomposition was performed with 100 mg of the catalyst placed in a fixed-bed plug flow-through microreactor in the temperature range 350–425 °C. The catalyst was pretreated in a helium stream at 450 °C for 2 h and then in an oxygen stream at 450 °C for 1 h. The feed contained 1000 ppm N₂O, 500 ppm NO, 3% O₂ and 1% H₂O in He (similar composition to that of the end-pipe gases in nitric acid plants) with a total flow rate of 300 ml min⁻¹, corresponding to GHSV 90,000 h⁻¹. Analysis of N₂O/NO/NO₂, N₂, and O₂ at the reactor outlet was performed using an Advanced Optima (ABB) IR analyzer, AH (MLU) chemiluminescence N₂O/NO_x analyzer, and Hewlett Packard 5890 II Gas chromatograph.

The rates of N₂O decomposition to N₂ and O₂, and NH₃-SCR-NO_x to N₂ over Fe-BEA* catalysts and of *n*-decane cracking over H-BEA were calculated from the conversions using the pseudo-first-order kinetic equation written as $r = F/W * (-\ln(1 - x))$, where F is the

flow rate of the feed (mol of N₂O or NO or *n*-decane per h) and W is the weight of the catalyst (kg), in agreement with the reported reaction rate first-orders with respect to N₂O [23], NO [24] and *n*-decane [25]. The TOF values were calculated for the respective reactions per Al, Brønsted OH, and Fe.

Small crystallites of BEA-5 and BEA-11 (~0.3–0.5 and ~0.05 μm, respectively) support their minimum contribution to the overall reaction rates for the flow rates (cf. the conditions given in Refs. [26,27]) employed in NH₃-SCR-NO_x, N₂O, decomposition and decane cracking. For the bulkier molecules participating in alkylation of benzene with benzyl alcohol and hydroamination of styrene with aniline, carried out in a liquid phase, diffusion constraints certainly decrease the measured reaction rates. As the BEA-5 zeolite exhibits small crystals that are, nevertheless, much larger than BEA-11, the higher conversions obtained over BEA-5 compared to those over BEA-11 cannot be explained by the diffusion effect.

3. Results and discussion

3.1. Synthesis and analysis of the structure of H-BEA

The beta zeolite with a low Si/Al molar ratio of 4.6 (BEA-5) was prepared by template-free synthesis and the use of seeding crystals. The obtained BEA-5 consisted of well-developed crystals 0.3–0.5 μm in size with a high surface area of 482 m² g⁻¹, mainly in micropores (470 m² g⁻¹), as estimated from the SEM images and adsorption isotherms of N₂ at 77 K (Fig. 3 and Table 1). BEA-11 exhibited a lower micropore surface area (333 m² g⁻¹) and higher external surface area (284 m² g⁻¹) due to its very small crystallites (~0.05 μm). The intensities and patterns of the X-ray diffraction lines for both BEA* zeolites are characteristic of the well-developed crystalline structure of BEA* topology formed by intergrowth of polymorphs A and B (Fig. 3; cf. Ref. [28]). The shift of all the reflections of ca. 0.3 2θ to the lower values observed for BEA-5 corresponds to a higher Al concentration than for BEA-11. Sharper and more intensive reflections of BEA-5 indicate highly regular structure and slightly larger crystals.

In contrast to other zeolites, the structure of beta zeolite is connected with a reversible change in the coordination of the framework Al atoms in the hydrated zeolite, depending on the type of counterion balancing the framework negative charge. It is generally accepted that part of the framework Al atoms (with tetrahedral coordination in Na form) exhibit octahedral coordination in the hydrated protonic form of the BEA* zeolite [29–35]. Thus, the coordination and local surroundings of the Al sites were analyzed by the ²⁷Al and ²⁹Si MAS NMR spectra of Na-beta zeolites shown in Fig. 4 and Supplement III. ²⁷Al single pulse MAS NMR spectra of both samples showed the presence of tetrahedral Al atoms reflected in the ²⁷Al resonance with the observed shift around 55 ppm, corresponding to the framework Al atoms. Resonances with ²⁷Al observed shifts around 0 ppm reflecting extraframework octahedral Al atoms, and shifts between 30 and 45 ppm attributable to extraframework penta-coordinated Al atoms or perturbed tetrahedral Al atoms (framework or extraframework), were not observed. The ²⁷Al 3Q MAS NMR experiment provides deeper insight into the local arrangement of the framework Al atoms in the zeolite. Two resonances can be recognized in the ²⁷Al 3Q MAS NMR spectra of both Na-BEA-5 and -11 (Fig. 4A). The predominant resonance with the ²⁷Al isotropic shift at 58.6 ppm (F1 = 59.5 ppm and F2 = 57.0 ppm) and a shoulder with a ²⁷Al isotropic shift at around 55.8 ppm (F1 = 56.5 ppm and F2 = 54.5 ppm) were observed. Both resonances are well known to be present in the ²⁷Al MAS NMR spectra of BEA* zeolites, and the ²⁷Al 3Q MAS NMR spectra of Na-BEA-5 and -11 do not differ from those already reported for Si-rich samples [36–39]. The only remarkable feature

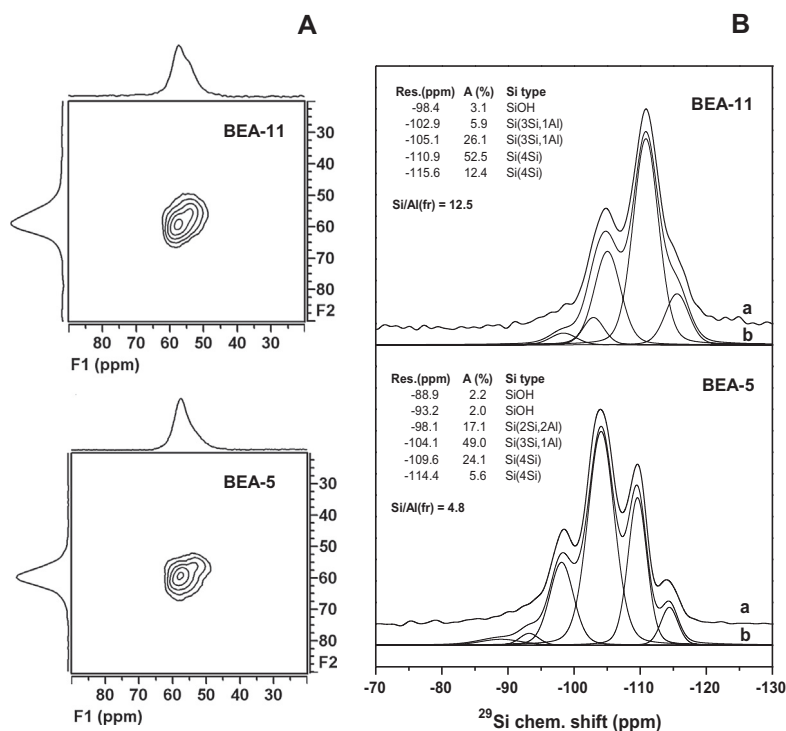


Fig. 4. MAS NMR spectra of hydrated Na-beta zeolites. (A) 2D plot and F1 and F2 projections of the ^{27}Al 3Q MAS NMR spectra and (B) ^{29}Si MAS NMR spectra with relative areas of the individual resonances and their attribution to $\text{Si}(x\text{Si}_y\text{Al})$ atoms: (a) experimental data and (b) Gaussian bands of the individual resonances.

that can be connected with the ^{27}Al MAS NMR spectrum of Na-BEA-5 is the low intensity of the resonance at 55.8 ppm. The relative intensity of this resonance was reported to increase with dealumination of the BEA⁺ samples, but assignment of both the resonances to the Al atom in a specific location is not yet clear. Quantitative analysis of the ^{29}Si MAS NMR spectra of both the hydrated Na-beta zeolites (Fig. 4B and Table 1) yielded framework Si/Al_{FR} ratios of 4.8 and 12.5 for BEA-5 and BEA-11, respectively, comparable with those obtained from the chemical analysis (see Table 1). Therefore, analysis of both the ^{27}Al and ^{29}Si MAS NMR spectra of Na-BEA-5 and Na-BEA-11 indicates well-developed regular BEA⁺ structures with a predominance of Al atoms in tetrahedral coordination in the framework. The ^{29}Si MAS NMR spectrum of BEA-11 is similar to those reported previously for beta zeolites (Si/Al > 11) synthesized using an organic template [16], indicating the only possible Al presence as that of Si(1Al3Si) atoms (Fig. 4) [17,38]. The spectrum of BEA-5 contains an additional resonance at -98.1 ppm representing Si(2Si,2Al) atoms in AlSiAl sequences with two next nearest neighboring Al atoms [31,40]. The spectral contribution of this Si resonance is 17%. In our previous study on a BEA-11 sample, analysis of the exchange capacity of bare Co(II) ions showed that the framework Al atoms were present in AlSiAl sequences in 6MRs and as single Al atoms located in different rings [16]. Therefore, the major differences between BEA-5 and BEA-11 are the high concentration of Al in the framework and the occurrence of AlSiAl sequences in the framework of BEA-5.

The strength of the bridging SiOHAl protonic sites in H-BEA-11 and also other Si-rich H-zeolites with Si/Al > 12 has been shown not to be affected by the concentration and distribution of Al atoms between AlSiAl sequences and single Al atoms [41]. However, it is well known that in Y zeolites with Si/Al ~ 3, with AlSiAl sequences the protonic sites are mutually affected and exhibit much lower acid strengths of the bridging OH groups [42]. Fig. 5 depicts the IR spectra in the region of the OH groups ($\nu(\text{O}-\text{H})$ vibration mode) for H-BEA-5 and H-BEA-11, which are typical for the OH vibrations

in the BEA⁺ zeolites [43]. In addition to the intensities of the individual IR vibrations, the zeolites differ in the position of the bands of the noninteracting bridging OH groups at 3614 and 3611 cm^{-1} , respectively. Both zeolites exhibited substantial intensities in a broad absorption range from 3620 to 3200 cm^{-1} , reflecting vibrations of interacting OH groups, a band at 3745 cm^{-1} of the terminal SiOH groups, and a low intensity around 3735 cm^{-1} , indicating inner SiOH in the defect sites [44]. H-BEA-5 possesses much higher intensity of both the noninteracting (3614 cm^{-1}) and mutually affected (3620–3200 cm^{-1}) bridging OH groups. The number of

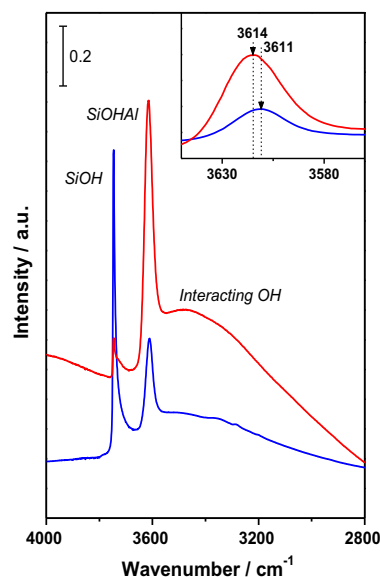


Fig. 5. FTIR spectra of H-BEA-5 (—) and H-BEA-11 (—) zeolites in the region of OH groups after evacuation at 450 °C with detail of the bands of Brønsted OH.

terminal SiOH groups (3745 cm^{-1}) was very small in BEA-5, compared with their high intensity for small crystallites and the high external surface area of BEA-11. Neither of the BEA^{*} zeolites exhibited extraframework Al–OH groups of vibrations at approx. 3650 cm^{-1} , supporting the presence of Al atoms in the framework sites.

Quantitative analysis of the IR intensities of the characteristic C≡N vibrations ($\nu(\text{C}\equiv\text{N})$ mode) of adsorbed d_3 -acetonitrile (spectrum not shown) distinguishing between Brønsted and Lewis sites indicated that H-BEA-5 contained approximately twice the concentration of Brønsted sites and a three times higher concentration of Lewis sites than H-BEA-11 (Table 1). While Na-BEA-5 with Al atoms charge-balanced by Na⁺ ions contained Al atoms exclusively in T_d coordination (absence of elevated intensity at 30–45 ppm and 0 ppm), the presence of Lewis sites in H-beta zeolites is not surprising, as the occurrence of unsaturated Al atoms (with electron acceptor properties) preserving their location in the framework as well as those in extraframework positions is typical of BEA^{*} topology [16,45]. If the Al atoms in H-BEA^{*} remain in the framework, the concentration of total framework Al (obtained from ²⁹Si MAS NMR, Table 1) should equal the sum of the concentration of Brønsted sites and twice the concentration of Lewis sites: $C_{\text{Al}} = C_{\text{B}} + 2C_{\text{L}}$. The obtained concentrations of Brønsted and Lewis sites for both BEA-5 and BEA-11 zeolites (Table 1, differences <8% from total Al concentrations) indicate that a highly predominant number of the Al atoms exhibiting a Lewis character preserve their location in the framework positions. The total Al content in BEA-5 increased ca. 2.2 times compared to BEA-11, while the concentrations of Brønsted and Lewis sites increased by 1.8 and 2.9 times, respectively. We can speculate that AlSiAl sequences present only in BEA-5 might be a particular reason for the increased concentration of Lewis sites.

Although the relationship between the shift in the frequency of the stretching vibration mode of bridging OH groups and the acid strength is not completely straightforward, the increase in the OH stretching frequency from 3611 to 3614 cm^{-1} for noninteracting SiOHAl groups of BEA-5 might reflect the lower strength of some Brønsted sites. For example, a shift in the OH vibrations of 10 and 20 cm^{-1} was reported by Chu and Chang [46] for evidently less acidic GaOHSi and FeOHSi groups, respectively, compared with the Al-substituted ZSM-5 framework. In this light, the shift of 3 cm^{-1} in the OH vibration does not indicate a significant change in the acid strength of the zeolite OH groups. It implies that, although the BEA-5 zeolite contains a substantially higher concentration of Al than BEA-11, its bridging OH groups preserved their high acid strength. Nevertheless, lower strength of some of the OH groups adjacent to AlSiAl sequences cannot be completely excluded.

The deprotonation energies of the Brønsted sites Al₁OHSi, Al₂OHSi, and Al₃OHSi were calculated for both the 15 and 5 models, corresponding to Si/Al 15 and 5.4, respectively (see Figs. 1 and 2), to estimate how the acid strength of the individual OH groups depends on Si/Al and the distribution of Al atoms in the framework. Our calculations for the 15 model for Al₁ and Al₂ forming Al₁-SiSiAl₂ (Fig. 2A, Table 2) show that the OH group belonging to Al₁ is free, while the other OH group of Al₂OHSi forms a hydrogen bond with the oxygen atom of a SiOSi chain in the 6MR. Our results reveal higher deprotonation energies for Al₁OHSi and Al₂OHSi in the 5 model of BEA-5 (ΔE_{DP} 6.6 and 3.7 kcal mol⁻¹, respectively) than in the same acidic sites in the 15 model of BEA-11 (Table 2), since both Al₁OHSi and Al₂OHSi yield hydrogen bonds with the oxygen atom of the SiOSi chains in the 5MR and 6MR, respectively. The higher deprotonation energy of the OH group belonging to Al₂ agrees with the fact that the corresponding hydrogen bond is stronger in the 5 model (the OH...O distance is 1.71 Å) than in the 15 model (the OH...O distance is 1.79 Å). It should be noted

that both the Al₁ and Al₂ atoms also form Al₁SiAl and Al₂SiAl sequences because of a higher number of Al atoms in the 5 model (Table 2). Two variants of the distribution of the framework Al atoms were employed in the 5 model, one with an Al₃ atom forming an Al₃SiAl chain (variant 1) and the other one with a single Al₃ atom (variant 2). Al₃ is a single Al atom in the 15 model and the corresponding Brønsted OH group yields a hydrogen bond with an oxygen atom of a SiOSi chain in the 6MR, whereas there is no such hydrogen bond in either of the variants of the 5 model. Despite the absence of a hydrogen bond in both variants, the deprotonation energy is slightly higher by 0.3 (single Al₃) and 1.1 (Al₃ in Al₃SiAl) kcal mol⁻¹ than that of the 15 model (Fig. 2B, Table 2).

The increase in the deprotonation energies for the 5 model relative to the 15 model (up to 6.6 kcal mol⁻¹) is smaller than the difference between the lowest and highest deprotonation energies calculated for the individual Brønsted sites of AlOHSi groups for the 15 model (i.e., $\Delta = 8.7\text{ kcal mol}^{-1}$ because $E_{\text{DP}} = 81.6$ (Al₁) and 90.3 (Al₂) kcal mol⁻¹). Thus calculations show that the strengths of the protonic acid sites in the 5 and 15 models does not significantly differ, being in the range of differences in the deprotonation energy values among the protons associated with AlOHSi groups at individual T sites of the framework. This finding is also consistent with the small shift in the OH stretching frequency in the FTIR spectra.

It can be concluded that the synthesized BEA-5 zeolite with Si/Al 4.6 with high concentration of Al located in T_d coordination in the framework is formed from small well-developed crystallites of BEA^{*} topology, without mesopores and of negligible external surface (~3%), unusually low compared to the conventional beta zeolites. To accommodate a high concentration of Al in the beta zeolite, in addition to AlSiAl sequences occurring in one ring and single Al atoms located in different rings in BEA-11, the AlSiAl sequences are formed in the framework of BEA-5. These sequences could lead to an increased fraction of Al atoms possessing electron-acceptor Lewis character in H-BEA-5, but still preserving the Al location in the framework. The acid strength of protons of the bridging OH groups as a total is high not significantly decreased, as supported by the very small shift in the structural OH vibrations and less-than-significant differences in the deprotonation energies for OH groups related to the individual Si–Al sequences.

3.2. Acid-catalyzed reactions

3.2.1. Cracking of *n*-decane

A linear relationship between the concentration of the bridging OH groups and the cracking rate was reported for beta and ZSM-5 zeolites [47,48]. Corma et al. [49] showed that the beta zeolite with Si/Al 12 provides slightly higher activity in cracking C₇–C₁₄ alkanes than the traditionally employed USY. They assumed that the absence of large cavities in the beta zeolite might be responsible for higher selectivity for olefins and lower rate of coke formation than with USY [49]. However, the necessity of using an expensive organic template for synthesis of the beta zeolite limits its use in large-scale catalytic cracking. Fig. 6 depicts the rate of *n*-decane cracking over H-BEA-5 compared with that of H-BEA-11 and a commercially employed H-USY-6. The reaction rate over H-BEA-5 is approximately twice as high as that over H-BEA-11 and H-USY-6. This is also reflected in the higher apparent activation energies for H-BEA-11. The TOF values calculated per Brønsted site at 500 °C are similar for H-BEA-5 (840 h⁻¹) and H-BEA-11 (833 h⁻¹), while those calculated per Al differ, being lower for H-BEA-5, as it contains a higher relative concentration of Lewis sites, which are assumed not to be active in decane cracking (Table 3). The selectivity of *n*-decane cracking to individual products was comparable for both H-BEA^{*} zeolites, as given in Supplement IV, with selectivity 41.1 and 42.0% for C₂–C₄ olefins, 30.6

Table 2

Deprotonation energies (E_{DP}) of the corresponding Brønsted acid sites for the calculated 15 (4 Al atoms in one unit cell, Si/Al 15) and 5 models (10 Al atoms in one unit cell, Si/Al 5.4).

AlOHSi group	The 15 model		The 5 model		ΔE_{DP} (kcal mol ⁻¹)
	Sequence	E_{DP} (kcal mol ⁻¹)	Sequence	E_{DP} (kcal mol ⁻¹)	
Al ₁ OHSi	Al ₁ SiSiAl ₂ in 6MR	81.6	Al ₁ SiSiAl ₂ in 6MR and Al ₃ SiAl	88.2	6.6
Al ₂ OHSi	Al ₁ SiSiAl ₂ in 6MR	90.3	Al ₁ SiSiAl ₂ in 6MR and Al ₂ SiAl	94.0	3.7
Al ₃ OHSi	Single Al ₃ in 6MR	86.8	Al ₃ SiAl ^{a,c}	87.9	1.1
			single Al ₃ ^{b,c}	87.1	0.3

^a Variant 1 of the 5 model with the Al₃ atom forming a Al₃SiAl sequence.

^b Variant 2 of the 5 model with the single Al₃ atom.

^c Both variants 1 and 2 feature the same location of Al₁SiSiAl₂.

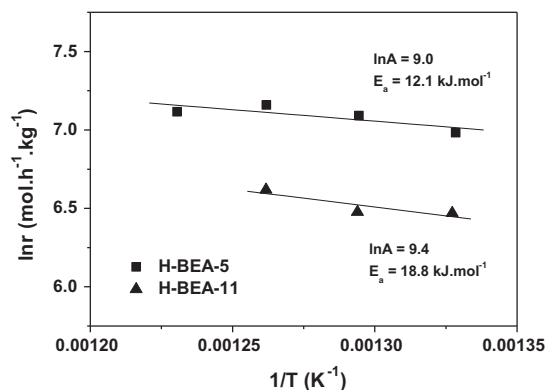


Fig. 6. Cracking of *n*-decane as a function of temperature over H-BEA-5 and H-BEA-11 shown as an Arrhenius plot with the pre-exponential factors ln A and activation energies.

and 29.5% for C₁–C₄ paraffins, and 28.2 and 28.5% for C₅⁺ hydrocarbons at comparable decane conversions of 76.3 and 80.6% for H-BEA-5 and H-BEA-11, respectively.

3.2.2. Alkylation of benzene with benzyl alcohol to diphenyl methane

A threefold increase in the conversion of benzyl alcohol (BzOH) was obtained with H-BEA-5 compared to H-BEA-11 (data for a reaction time of 2 h are shown in Fig. 7A, accompanied by a substantial increase in the selectivity for diphenylmethane (DPM), from 16.6% to 39.6% after 2 h, and half selectivity for dibenzyl ether (DBE), but twice the increase in selectivity for dibenzylated benzene (DBB); see Scheme 1 and Fig. 7A). Data for reaction times of 4 h and 24 h are given in Supplement IV. The increase in conversion of BzOH over H-BEA-5 and in selectivity for DPM and DBB (and the decrease in the selectivity for DBE) can be explained by an increase in the concentration of Brønsted and Lewis sites (cf. Table 1). Some of the increase in the yield of the desired DPM might also be explained by the reaction taking place inside pores

of larger crystallites of H-BEA-5 with predominant microporous surface (97% of the total surface area) in contrast to that in H-BEA-11 exhibiting high external surface area (see Table 1). When an excess of benzene (benzene/BzOH 2.5) was used (Fig. 7A), a further increase in the conversion of BzOH up to 85% and high selectivity (56.6%) for DPM were achieved. After 24 h, even in an excess of benzene, the conversion increased to 99% and the selectivity for DPM remained almost unchanged. In addition, no significant change in the activity was observed in three successive regeneration cycles (Supplement V).

3.2.3. Hydroamination of styrene with aniline

Scheme 2 illustrates amination of styrene by aniline to phenyl-[2-phenylethyl]amine and phenyl-[1-phenylethyl]amine. Fig. 7B shows high conversion of aniline in styrene hydroamination (87%) with high selectivity for the Markovnikov isomer (68%) over H-BEA-5, markedly exceeding the aniline conversion over H-BEA-11 (16%) with Markovnikov selectivity of 58%. To the best of our knowledge, the H-BEA-5 zeolite provides the highest yields in phenyl-[2-phenylethyl]amine and phenyl-[1-phenylethyl]amine reported for this reaction in the literature to date (cf., e.g., Ref. [50], where the maximum conversion was 75%, with selectivity for the Markovnikov isomer of 35% under the same conditions). In Ref. [50], analyzing the activity and regioselectivity in beta zeolites, the Brønsted acid sites were assumed to orient the hydroamination toward the *anti*-Markovnikov adducts, while the Lewis acid sites oriented it towards Markovnikov regioisomers. While more than a fourfold increase in aniline conversion can be attributed to an increase in the concentration of acid sites, the higher regioselectivity for the Markovnikov adduct is not correlated with an increase in the relative concentration of Lewis sites in H-BEA-5 compared to H-BEA-11. It can be speculated that for the amination reaction occurring in the pores of BEA⁺ zeolites, other parameters might also contribute to the regioselectivity. Structure-directed shape selectivity with respect to regioisomers (cf. Ref. [51]) might play some role inside zeolite pores.

Table 3

Cracking of *n*-decane over H-BEA-5 compared to H-BEA-11 and H-USY-6 (Si/Al 6, Zeolyst Int. CBV712, Lot 712014001708).

Sample	T (°C)	Conversion of C ₁₀ H ₂₂ (%)	r^a (mol _{C₁₀H₂₂} kg _{cat} ⁻¹ h ⁻¹)	TOF ^b (mol _{C₁₀H₂₂} mol _{OH} ⁻¹ h ⁻¹)	TOF ^c (mol _{C₁₀H₂₂} mol _{Al} ⁻¹ h ⁻¹)
H-BEA-11	480	53.8	645	–	478
	500	54.1	650	833	481
	520	59.2	748	–	554
H-BEA-5	480	72.5	1077	–	363
	500	76.3	1201	840	404
	520	78.6	1286	–	433
H-USY-6	480	44.9	498	–	209
	500	43.8	481	–	202
	520	55.5	676	–	284

^a Reaction rate calculated from the first-order kinetics.

^b TOF per Brønsted OH group.

^c TOF per Al.

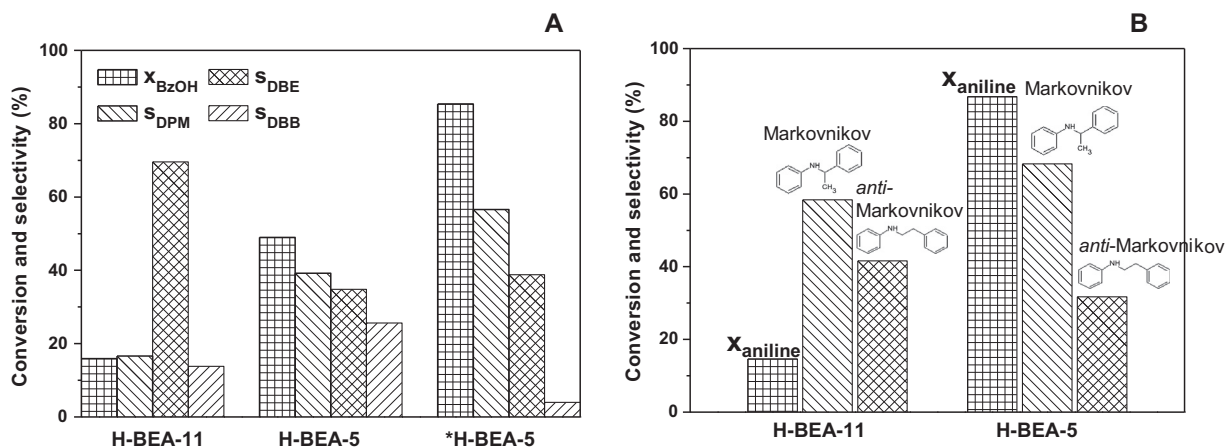
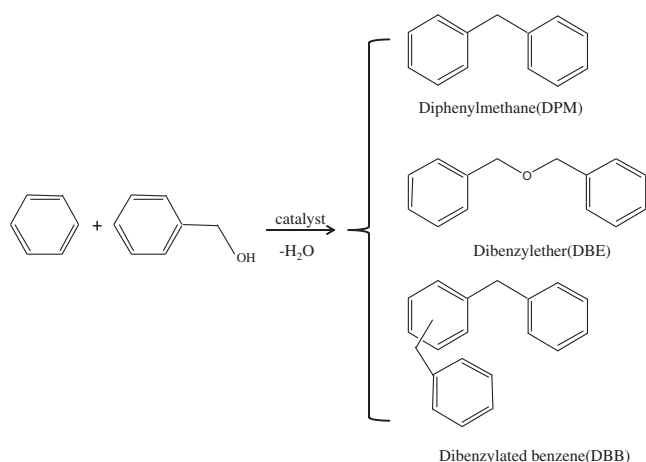
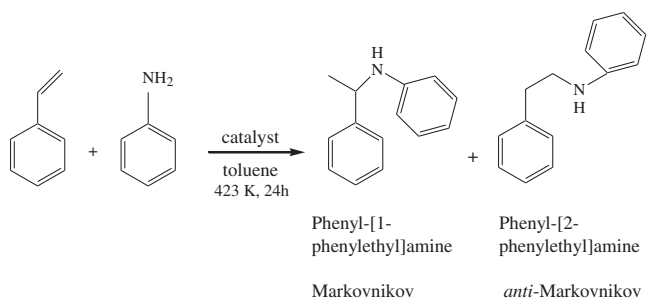


Fig. 7. Activity of H-BEA-5 in acid-catalyzed reactions compared to H-BEA-11. (A) Conversion of benzyl alcohol (x_{BzOH}) in alkylation of benzene and selectivity to diphenyl methane (DPM) and by-products dibenzyl ether (DBE) and dibenzylated benzene (DBB) at benzene/BzOH 1 after 2 h. (*Excess of benzene at benzene/BzOH 2.5.) (B) Conversion of aniline (x_{aniline}) in hydroamination of styrene and selectivity for Markovnikov and *anti*-Markovnikov products.



Scheme 1. Alkylation of benzene with benzyl alcohol.



Scheme 2. Hydroamination of styrene with aniline.

3.3. Structure analysis and redox-catalyzed reactions over Fe-BEA*

Fe counterion species charge-balanced by the framework AlO_4^- in Si-rich zeolites are known to be highly active sites in $\text{NH}_3\text{-SCR-NO}_x$ [4] and decomposition of N_2O to molecular N_2 and O_2 [52]. Increased Fe(II) ion-exchange capacity of BEA-5 for counterion Fe species similar to those in traditional Si-rich Fe-BEA* was assumed. The Fe(II) ion exchange occurred under a non-oxidizing atmosphere, but exposure of Fe-BEA* in a hydrated state to air oxidized a predominant part of Fe(II) to Fe(III) species. UV-vis-NIR spectra monitored for estimation of the state of Fe species

in the resulting Fe-BEA-5 compared to Fe-BEA-11 exhibited significantly higher intensities of the $\text{O} \rightarrow \text{Fe(III)}$ ligand to metal charge transfer (LMCT) at 36,000–48,000 and 28,000 cm^{-1} connected with isolated Fe(III)-oxo species with T_d and O_h coordination [53] and bridging or polynuclear Fe(III)-oxo complexes [27,54], respectively (Fig. 8). The possible presence of Fe(II) species [26,27] was not detected in the vis range because of the low intensities of their $d-d$ transitions [26] and their overlap in the MLCT region. Although various Fe(III) species could not be analyzed quantitatively because of lack of knowledge of the extinction coefficients of the individual LMCT transitions, the spectral intensities indicate a significantly higher population of counterion Fe species in Fe-BEA-5 compared to Fe-BEA-11. This corresponds to differences in Fe content (11.7 and 5.3 wt.%, respectively) and in the content of framework Al atoms in the beta zeolites (Table 1). The increased ion-exchange capacity of Fe-BEA-5 is also supported by the lower intensity of the absorption, around 18,000 cm^{-1} in Fe-BEA-5 compared to Fe-BEA-11, reflecting the lower concentration of small Fe oxide-like neutral species not charge-balanced by the negative framework in Fe-BEA-5.

As Fe-catalysts undergo severe hydrothermal treatment, particularly in the SCR- NO_x process in active diesel engine exhaust systems, the UV-vis-NIR spectra were monitored also on Fe-BEA* pretreated in 10% H_2O at 600 °C for 12 h. This resulted in a lower

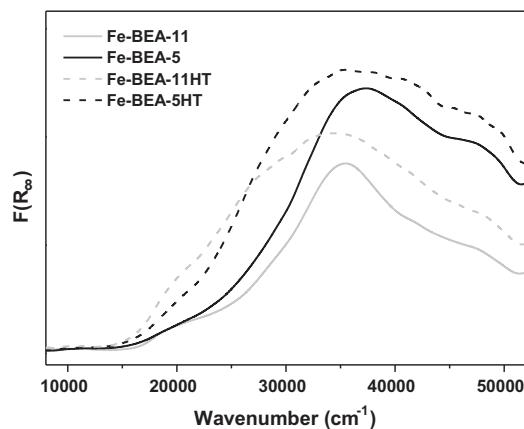


Fig. 8. Diffuse reflectance UV-vis-NIR spectra of hydrated Fe-BEA-5 and Fe-BEA-11 catalysts and catalysts treated in a stream of 10% water vapor at 600 °C for 12 h (Fe-BEA-5HT and Fe-BEA-11HT).

degree of clustering of counterion Fe species into Fe-oligomers and formation of inactive Fe oxides in H-BEA-5 compared to Fe-BEA-11, reflected in the lower relative band intensities at $\sim 18,000\text{ cm}^{-1}$ and preservation of a large portion of the counterion Fe species manifested by the absorption in the region $28,000\text{--}48,000\text{ cm}^{-1}$. These findings indicate better stabilization of a high concentration of counterion Fe species and framework Al in Fe-BEA-5 under the severe conditions of hydrothermal calcination.

3.3.1. $\text{NH}_3\text{-SCR-NO}_x$ and decomposition of N_2O over Fe-BEA*

Fig. 9 depicts the temperature dependence of NO conversion to N_2 , pseudo-first-order reaction rates, and Arrhenius plots for the $\text{NH}_3\text{-SCR-NO}_x$ reaction over Fe-BEA-5 and Fe-BEA-11 and the catalysts pretreated in a stream of 10% H_2O in He at $600\text{ }^\circ\text{C}$ for 12 h. The high concentration of Fe counterion species in Al-rich Fe-BEA-5 caused greatly improved conversion of NO_x over the low temperature range from 200 to $300\text{ }^\circ\text{C}$, important for catalyst application in diesel exhaust gases. The rates for conversion of NO_x to N_2 over Fe-BEA-5 and steamed Fe-BEA-5HT catalysts (Fig. 9B) are more than twice as high as those of Fe-BEA-11 and Fe-BEA-11HT, respectively. A similar activity increase in $\text{NH}_3\text{-SCR-NO}_x$ over the Al-rich Fe-BEA is reported in the recent patent assigned to BASF [55]. The apparent activation energies obtained from the Arrhenius plots (Fig. 9C) for all the Fe catalysts investigated here range from 40 to 47 kJ mol^{-1} , in agreement with those reported in the literature for Fe species in zeolites ($E_a = 36\text{--}51\text{ kJ mol}^{-1}$ in the temperature range $200\text{--}300\text{ }^\circ\text{C}$ [24,26,56]). However, E_a over Fe-BEA-5 are compensated for by a pre-exponential factor A ($\ln A$ from -1 up to 2.6) several orders of magnitude higher for the most active Fe-BEA-5 catalyst. This can be seen on similar types of active counterion Fe sites, and the higher activity of Fe-BEA-5 is caused by their higher concentration. This assumption is clearly evident from equal TOF_{SCR} values (per Fe) obtained over Fe-BEA-5 and Fe-BEA-11 in the whole temperature range studied (Table 4).

The effect of a high concentration of Al in the framework and a corresponding high concentration of counterion Fe sites is also manifested in the decomposition of N_2O to N_2 and O_2 (note that this is in the presence of NO), depicted for Fe-BEA-5 and Fe-BEA-11 in Fig. 10. Pseudo-first-order kinetic plots with respect to N_2O [23] and zero-order plots with respect to N_2 and O_2 [57] ($-\ln(1-x) = r_{\text{N}_2\text{O}}(W/F)$) were used to obtain the reaction rate for temperatures of $350\text{--}425\text{ }^\circ\text{C}$ (Fig. 10A). An approximately one and one-half times higher rate of N_2O decomposition over Fe-BEA-5 than over Fe-BEA-11 was obtained (Fig. 10B). The apparent activation energies of 125 and 132 kJ mol^{-1} for Fe-BEA-5 and Fe-BEA-11, respectively, are slightly lower than 140 kJ mol^{-1} reported for N_2O decomposition in the presence of NO over Fe-ZSM-5 zeolites [58]. The E_a value is slightly higher for the more active Fe-BEA-5, but it is compensated for by the approximately two-order-higher pre-exponential factor A ($\ln A = 16$ vs. 14). Not so for $\text{NH}_3\text{-SCR-NO}_x$, where identical TOF_{SCR} values per Fe were found in both Fe-BEA* catalysts. The $\text{TOF}_{\text{deN}_2\text{O}}$ per Fe over Fe-BEA-5 reached roughly only 70% of that over Fe-BEA-11 (Table 4). This implies that the concentration of the Fe sites most active in N_2O decomposition did not follow in linear proportionality the increase in the Al concentration of BEA-5. The most active sites for N_2O decomposition over Fe-MFI, Fe-FER, and Fe-BEA* have been identified as bare Fe(II) ions, whose divalent state is stabilized by an Al-Si-Si-Al sequence in 6MRs, even in the oxidizing atmosphere present during the decomposition reaction [26,27,59–62]. The increased activity in N_2O decomposition with Fe-BEA-5 reported here can be attributed to the increased concentration of these Fe ions, but it does not strictly correspond to the increase in the concentration of framework aluminum.

For both $\text{NH}_3\text{-SCR-NO}_x$ and N_2O decomposition, the use of Fe-BEA-5 containing an increased concentration of counterion Fe species is clearly beneficial. Nevertheless, while the sum of concentrations of all types of counter Fe ions and Fe-oxo species active in

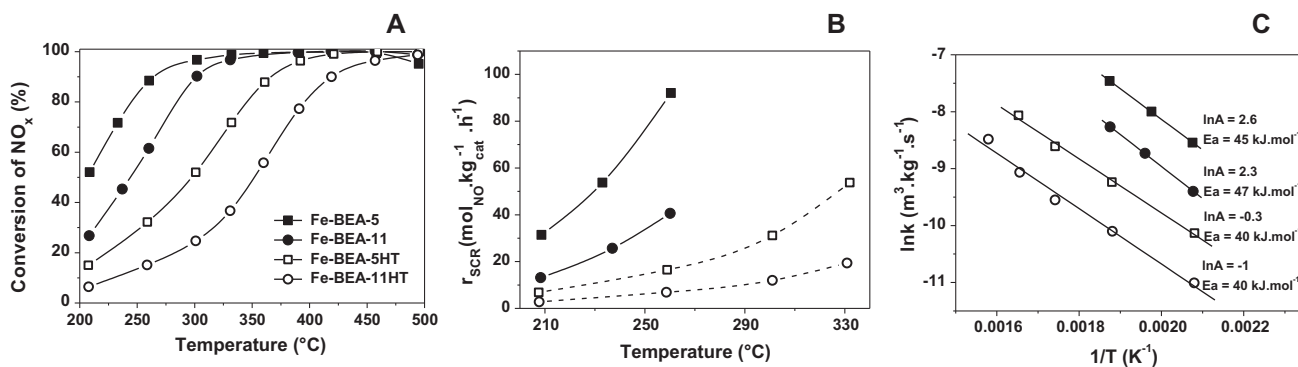


Fig. 9. $\text{NH}_3\text{-SCR-NO}_x$ over Fe-BEA-5 and Fe-BEA-11 and catalysts treated in a stream of 10% H_2O in He at $600\text{ }^\circ\text{C}$ for 12 h (Fe-BEA-5HT and Fe-BEA-11HT). Reaction conditions: 490 ppm NO , 520 ppm NH_3 , 2% O_2 in He, GHSV $510,000\text{ h}^{-1}$. (A) Conversion of NO_x as a function of temperature. (B) First-order reaction rate r_{SCR} as a function of temperature. (C) Arrhenius plot with the pre-exponential factors $\ln A$ and apparent activation energies.

Table 4

Composition of Fe-BEA* and TOF and reaction rate r for $\text{NH}_3\text{-SCR-NO}_x$ and decomposition of N_2O .

Sample	c_{Fe} (wt.%)	Fe/ Al	$\text{NH}_3\text{-SCR-NO}$				Decomposition of N_2O			
			210 $^\circ\text{C}$		260 $^\circ\text{C}$		400 $^\circ\text{C}$		425 $^\circ\text{C}$	
			r^a ($\text{mol}_{\text{NO}}\text{ kg}^{-1}\text{ h}^{-1}$)	TOF^b (h^{-1})	r^a ($\text{mol}_{\text{NO}}\text{ kg}^{-1}\text{ h}^{-1}$)	TOF^b (h^{-1})	r^a ($\text{mol}_{\text{N}_2\text{O}}\text{ kg}^{-1}\text{ h}^{-1}$)	TOF^c (h^{-1})	r^a ($\text{mol}_{\text{N}_2\text{O}}\text{ kg}^{-1}\text{ h}^{-1}$)	TOF^c (h^{-1})
Fe-BEA-5	11.7	0.73	31.4	15.0	92.1	43.9	1.60	0.76	3.80	1.81
Fe-BEA-11	5.3	0.77	13.2	13.9	40.6	42.8	1.05	1.10	2.43	2.54

^a Reaction rate calculated from the first-order kinetics.

^b TOF ($\text{mol}_{\text{NO}}\text{ mol}_{\text{Fe}}^{-1}\text{ h}^{-1}$).

^c TOF ($\text{mol}_{\text{N}_2\text{O}}\text{ mol}_{\text{Fe}}^{-1}\text{ h}^{-1}$).

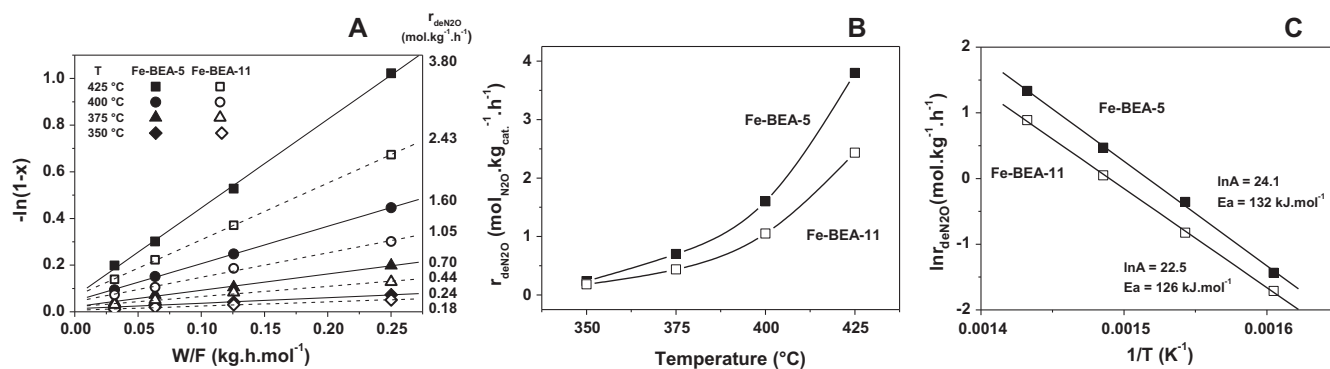


Fig. 10. Decomposition of N_2O over Fe-BEA-5 and Fe-BEA-11. Reaction conditions: 1000 ppm N_2O , 500 ppm NO , 3% O_2 , and 1% H_2O in He, GHSV 90,000 h^{-1} . (A) Pseudo-first-order kinetic plot $-\ln(1-x) = r_{\text{deN}_2\text{O}}(W/F)$. (B) First-order reaction rates $r_{\text{deN}_2\text{O}}$ as a function of temperature. (C) Arrhenius plot with the pre-exponential factors $\ln A$ and apparent activation energies.

$\text{NH}_3\text{-SCR-NO}_x$ is proportional to the increased concentration of framework Al, for the most active sites in N_2O decomposition, i.e., bare Fe(II) ions balanced by AlSiAl sequences in 6MRs, this relationship does not quantitatively follow the concentration of Al in the framework. This observation implies differences in the distribution of framework Al atoms in Fe-BEA-5 and Fe-BEA-11 balancing individual Fe counterion species. That is also indicated by the presence of AlSiAl sequences found in BEA-5 (cf. Si(2Al2Si) atoms in Fig. 4) in contrast to BEA-11 containing only AlSiAl sequences in 6MRs and single Al atoms, as reported in Ref. [16]. It might be speculated that the presence of AlSiAl sequences matches the occurrence of AlSiAl sequences in 6MRs charge balancing bare Fe(II) ions active in N_2O decomposition, but that they take part in charge balancing various counter Fe-oxo up to oligomeric Fe-oxo species active in $\text{NH}_3\text{-SCR-NO}_x$. However, the detailed description of the distribution of Al atoms in the framework of Al-rich BEA⁺ and its consequence for divalent ion-exchange capacity will be matters for further study.

4. Conclusions

The high concentration of Al in the framework of the template-free synthesized beta zeolite (Si/Al 4.6) compared with conventional Si-rich beta zeolite (Si/Al 11.3) provides charge balance for the corresponding high concentration of protons and/or counter divalent or trivalent oxo metal ion species. In addition to the high content of framework Al, the synthesized crystals of Al-rich beta zeolite (0.3–0.5 μm) exhibit highly regular pore structure with negligible external surface area, implying high shape selectivity effects of inner pores compared to very small crystallites (nm range) of Si-rich beta zeolites that commonly exhibit large external surfaces.

Although a much higher concentration of protonic sites is present in the Al-rich beta zeolite associated with AlO_4^- , these Brønsted sites represent strongly acidic sites of strength comparable to that of the protons of Si-rich beta zeolites. Nevertheless, some AlO_4^- exhibit an increased tendency toward perturbation of the T-O framework bonds with formation of Al-Lewis electron-acceptor sites, but preserving their location in the framework. These findings are manifested in the increased conversion in *n*-decane cracking, alkylation of benzene with benzyl alcohol to diphenylmethane, and hydroamination of styrene with aniline to phenyl-[2-phenylethyl]amine and phenyl-[1-phenylethyl]amine, correspondingly to the increased concentration of Brønsted acid sites. The differences in Al distribution between conventional H-BEA⁺ (containing only AlSiAl pairs and single Al atoms) and Al-rich H-BEA⁺ (possessing also AlSiAl sequences) are not significantly reflected in the acid strength and activity per Brønsted site. The increased

selectivity towards formation of diphenyl methane at the expense of diphenyl ether corresponds to the increased concentration of Brønsted sites.

An advantage of a high concentration of framework Al atoms in Al-rich BEA⁺ also lies in an increased concentration of counter Fe ion species with exceptional redox behavior reflected in the increased rates of N_2O decomposition and $\text{NH}_3\text{-SCR-NO}_x$ to molecular nitrogen. While the concentration of Fe-oxo and oligomeric Fe-oxo counter species active in $\text{NH}_3\text{-SCR-NO}_x$ followed the increased concentration of framework Al atoms, the N_2O decomposition occurring over bare Fe(II) ions is not strictly proportional to the increased Al concentration in Al-rich BEA⁺.

Beside the advantage of Al-rich beta zeolite with high ion-exchange capacity for protons and/or metal, metal-oxo ion species, it brings about the advantage of the less costly demanded synthesis without employing an organic template and typical highly regular crystals with high surface area of inner pores and negligible external surface area. That presumes enhanced exploiting of the shape selectivity of the three-dimensional 12MRs pores, particularly in reactions of bulkier organic molecules.

Acknowledgments

This study was supported by the Czech Science Foundation (Projects # P106/11/0624 and # GA14-10251S), by the Technology Agency of the Czech Republic (Project # TA01021377) and by RVO # 61388955.

Appendix A. Supplementary material

Supplementary data associated with this article can be found, in the online version, at <http://dx.doi.org/10.1016/j.jcat.2014.06.024>.

References

- [1] A. Corma, *Chem. Rev.* 95 (1995) 559–614.
- [2] D.E. De Vos, M. Dams, B.F. Sels, P.A. Jacobs, *Chem. Rev.* 102 (2002) 3615–3640.
- [3] F. Kapteijn, J. Rodriguez-Mirasol, J.A. Moulijn, *Appl. Catal., B: Environ.* 9 (1996) 25–64.
- [4] S. Brandenberger, O. Krocher, A. Tissler, R. Althoff, *Catal. Rev. Sci. Eng.* 50 (2008) 492–531.
- [5] Y. Traa, B. Burger, J. Weitkamp, *Microporous Mesoporous Mater.* 30 (1999) 3–41.
- [6] Ch. Baerlocher, L.B. McCusker, D.H. Olson, *Atlas of Zeolite Framework Types*, 6th revised edition, 2007.
- [7] B. Xie, J. Song, L. Ren, Y. Ji, J. Li, F.S. Xiao, *Chem. Mater.* 20 (2008) 4533–4535.
- [8] G. Majano, L. Delmotte, V. Valtchev, S. Mintova, *Chem. Mater.* 21 (2009) 4184–4191.
- [9] Y. Kamimura, S. Tanahashi, K. Itabashi, A. Sugawara, T. Wakihara, A. Shimajima, T. Okubo, *J. Phys. Chem. C* 115 (2011) 744–750.
- [10] Y. Kubota, K. Itabashi, S. Inagaki, Y. Nishita, R. Komatsu, Y. Tsuboi, S. Shinoda, T. Okubo, *Chem. Mater.* 26 (2014) 1250–1259.

- [11] B. Yilmaz, U. Muller, M. Feyen, S. Maurer, H. Zhang, X. Meng, F.S. Xiao, X. Bao, W. Zhang, H. Imai, T. Yokoi, T. Tatsumi, H. Gies, T. De Baerdemaeker, D. De Vos, *Catal. Sci. Technol.* 3 (2013) 2580–2586.
- [12] T. De Baerdemaeker, B. Yilmaz, U. Muller, M. Feyen, F.S. Xiao, W. Zhang, T. Tatsumi, H. Gies, X. Bao, D. De Vos, *J. Catal.* 308 (2013) 73–81.
- [13] P. Sazama, Z. Sobalik, J. Dedecek, I. Jakubec, V. Parvulescu, Z. Bastl, J. Rathousky, H. Jirglova, *Angew. Chem., Int. Ed.* 52 (2013) 2038–2041.
- [14] H. Zhang, B. Xie, X. Meng, U. Muller, B. Yilmaz, M. Feyen, S. Maurer, H. Gies, T. Tatsumi, X. Bao, W. Zhang, D. De Vos, F.S. Xiao, *Microporous Mesoporous Mater.* 180 (2013) 123–129.
- [15] E.J. Creghton, S.D. Ganeshie, R.S. Downing, H. Van Bakkum, *J. Mol. Catal. A: Chem.* 115 (1997) 457–472.
- [16] L. Capek, J. Dedecek, P. Sazama, B. Wichterlova, *J. Catal.* 272 (2010) 44–54.
- [17] C.A. Fyfe, Y. Feng, H. Grondey, G.T. Kokotailo, H. Gies, *Chem. Rev.* 91 (1991) 1525–1543.
- [18] B. Wichterlova, Z. Tvaruzkova, Z. Sobalik, P. Sarv, *Microporous Mesoporous Mater.* 24 (1998) 223–233.
- [19] K. Klier, *J. Opt. Soc. Am.* 62 (1972) 882.
- [20] M. Brandle, J. Sauer, *J. Am. Chem. Soc.* 120 (1998) 1556–1570.
- [21] U. Eichler, M. Brandle, J. Sauer, *J. Phys. Chem. B* 101 (1997) 10035–10050.
- [22] J. Sauer, *J. Mol. Catal.* 54 (1989) 312–323.
- [23] F. Kapteijn, G. Marban, J. Rodriguez-Mirasol, J.A. Moulijn, *J. Catal.* 167 (1997) 256–265.
- [24] S. Brandenberger, O. Krocher, A. Tissler, R. Althoff, *Appl. Catal., B: Environ.* 95 (2010) 348–357.
- [25] L. Riekerti, J.Q. Zhou, *J. Catal.* 137 (1992) 437–452.
- [26] P. Sazama, B. Wichterlova, E. Tabor, P. Stastny, N.K. Sathu, Z. Sobalik, J. Dedecek, S. Sklenak, P. Klein, A. Vondrova, *J. Catal.* 312 (2014) 123–138.
- [27] P. Sazama, N.K. Sathu, E. Tabor, B. Wichterlova, S. Sklenak, Z. Sobalik, *J. Catal.* 299 (2013) 188–203.
- [28] M.M.J. Treacy, J.M. Newsam, *Nature* 332 (1988) 249–251.
- [29] E. Bourgeat-Lami, P. Massiani, F. Di Renzo, P. Espiau, F. Fajula, T. Des Courieres, *Appl. Catal.* 72 (1991) 139–152.
- [30] L.W. Beck, J.F. Haw, *J. Phys. Chem.* 99 (1995) 1076–1079.
- [31] R.B. Borade, A. Clearfield, *Microporous Mater.* 5 (1996) 289–297.
- [32] L.C. De Menorval, W. Buckermann, F. Figueras, F. Fajula, *J. Phys. Chem.* 100 (1996) 465–467.
- [33] P.J. Kunkeler, B.J. Zuurdeeg, J.C. Van Der Waal, J.A. Van Bokhoven, D.C. Koningsberger, H. Van Bakkum, *J. Catal.* 180 (1998) 234–244.
- [34] G.H. Kuehl, H.K.C. Timken, *Microporous Mesoporous Mater.* 35–36 (2000) 521–532.
- [35] J. Penzien, A. Abraham, J.A. Van Bokhoven, A. Jentys, T.E. Muller, C. Sievers, J.A. Lercher, *J. Phys. Chem. B* 108 (2004) 4116–4126.
- [36] J.A. Van Bokhoven, D.C. Koningsberger, P. Kunkeler, H. Van Bakkum, A.P.M. Kentgens, *J. Am. Chem. Soc.* 122 (2000) 12842–12847.
- [37] D.M. Roberge, H. Hausmann, W.F. Holderich, *Phys. Chem. Chem. Phys.* 4 (2002) 3128–3135.
- [38] L. Capek, J. Dedecek, B. Wichterlova, *J. Catal.* 227 (2004) 352–366.
- [39] J. Dedecek, S. Sklenak, C. Li, F. Gao, J. Brus, Q. Zhu, T. Tatsumi, *J. Phys. Chem. C* 113 (2009) 14454–14466.
- [40] J. Perez-Pariente, J. Sanz, V. Fornes, A. Corma, *J. Catal.* 124 (1990) 217–223.
- [41] P. Sazama, J. Dedecek, V. Gabova, B. Wichterlova, G. Spoto, S. Bordiga, *J. Catal.* 254 (2008) 180–189.
- [42] N. Wang, M. Zhang, Y. Yu, *Microporous Mesoporous Mater.* 169 (2013) 47–53.
- [43] C. Paze, S. Bordiga, C. Lamberti, M. Salvalaggio, A. Zecchina, G. Bellussi, *J. Phys. Chem. B* 101 (1997) 4740–4751.
- [44] P. Sazama, B. Wichterlova, J. Dedecek, Z. Tvaruzkova, Z. Musilova, L. Palumbo, S. Sklenak, O. Gonsiorova, *Microporous Mesoporous Mater.* 143 (2011) 87–96.
- [45] I. Kiricsi, C. Flego, G. Pazzuconi, W.O. Parker, R. Millini, C. Perego, G. Bellussi, *J. Phys. Chem.* 98 (1994) 4627–4634.
- [46] C.T.W. Chu, C.D. Chang, *J. Phys. Chem.* 89 (1985) 1569–1571.
- [47] S. Kottrel, M.P. Rosynek, J.H. Lunsford, *J. Catal.* 182 (1999) 278–281.
- [48] A.F.H. Wielers, M. Vaarkamp, M.F.M. Post, *J. Catal.* 127 (1991) 51–66.
- [49] A. Corma, P.J. Miguel, A.V. Orchilles, *Appl. Catal., A: Gen.* 138 (1996) 57–73.
- [50] M. Ciobanu, A. Tirsoaga, P. Amoros, D. Beltran, S.M. Coman, V.I. Parvulescu, *Appl. Catal., A: Gen.* 474 (2014) 230–235.
- [51] B. Wichterlova, J. Cejka, *J. Catal.* 146 (1994) 523–529.
- [52] G.D. Pirngruber, M. Luechinger, P.K. Roy, A. Cecchetto, P. Smirniotis, *J. Catal.* 224 (2004) 429–440.
- [53] S. Bordiga, R. Buzzoni, F. Geobaldo, C. Lamberti, E. Giamello, A. Zecchina, G. Leofanti, G. Petrini, G. Tozzola, G. Vlaic, *J. Catal.* 158 (1996) 486–501.
- [54] G.D. Pirngruber, P.K. Roy, R. Prins, *Phys. Chem. Chem. Phys.* 8 (2006) 3939–3950.
- [55] S. Maurer, M. Wycisk, J. Petry, S. Deuerlein, W. Zhang, Ch. Shi, H. Takashi, *WO2013118063*.
- [56] M. Iwasaki, K. Yamazaki, H. Shinjoh, *Appl. Catal., A: Gen.* 366 (2009) 84–92.
- [57] K. Sun, H. Xia, E. Hensen, R. Van Santen, C. Li, *J. Catal.* 238 (2006) 186–195.
- [58] H. Xia, K. Sun, Z. Liu, Z. Feng, P. Ying, C. Li, *J. Catal.* 270 (2010) 103–109.
- [59] J. Dedecek, L. Capek, P. Sazama, Z. Sobalik, B. Wichterlova, *Appl. Catal., A: Gen.* 391 (2011) 244–253.
- [60] Z. Sobalik, J. Novakova, J. Dedecek, N.K. Sathu, E. Tabor, P. Sazama, P. Stastny, B. Wichterlova, *Microporous Mesoporous Mater.* 146 (2011) 172–183.
- [61] Z. Sobalik, P. Sazama, J. Dedecek, B. Wichterlova, *Appl. Catal., A: Gen.* 474 (2014) 178–185.
- [62] E. Tabor, K. Zaveta, N.K. Sathu, A. Vondrova, P. Sazama, Z. Sobalik, *Catal. Today* 175 (2011) 238–244.